Optically Reconfigurable Graphene/Metal Metasurface on Fe:LiNbO$_3$ for Adaptive THz Optics

Jon Gorecki,[*,†] Lewis Piper,[‡] Adnane Noual,[¶] Sakellaris Mailis,[§] Nikitas Papasimakis,[†] and Vasilis Apostolopoulos[‡]

†*Optoelectronics Research Centre, University of Southampton, Southampton, SO17 1BJ, UK*

‡*School of Physics and Astronomy, University of Southampton, Southampton, SO17 1BJ, UK*

¶*LPMR, Department of Physics, FPN, University Mohammed Premier, Oujda 60000, Morocco.*

§*Skolkovo Institute of Science and Technology, Moscow 143026, Russia*

E-mail: J.Gorecki@soton.ac.uk

Abstract

We demonstrate, experimentally, non-volatile optical control of terahertz metasurfaces comprising of a metallic split ring resonator array sandwiched between monolayer graphene and a photoconductive Fe:$LiNbO_3$ substrate. We demonstrate frequency selective tuning of THz transmission amplitude, and our results pave the way towards spatially resolved control of THZ metasurfaces for beam-steering, imaging, and sensing applications. The substrate (Fe:$LiNbO_3$) supports non-volatile yet reversible photoinduced charge distributions, which locally modify the electrostatic environment of the nano-thickness graphene monolayer, altering the graphene electrical conductivity and therefore changing the resonance spectra of the metamaterial array. We present light-induced normalized transmittance changes up to 35% that are non-volatile and persist after the illumination source is removed, yet can be reversed by thermal annealing.

Keywords

Tunable, Metamaterials, Plasmonic, Lithium Niobate, Terahertz, 2D Materials, Non-Volatile

1 Introduction

Terahertz frequencies show potential for technological applications in a wide range of areas, such as spectroscopy of biological samples,[1–4] detection of concealed drugs and explosives,[5–7] imaging of astronomical objects,[8,9] industrial quality control of semiconductor manufacturing,[10,11] and broad bandwidth telecommunications systems.[12,13] Despite this wide array of applications, there is a lack of optoelectronic devices for the tuning of phase, amplitude, and polarisation of terahertz radiation. To this end a variety of tuning techniques based on optical,[14–16] thermal,[17,18] electronic,[19–21] and mechanical[22,23] actuation have been developed. Optical actuation methods generally offer an advantage over other approaches in that they readily allow for large areas of the tuning device to be addressed in parallel and with micron-scale spatial resolution, although such mechanisms are typically volatile. Early demonstrations relied on optically excited charge carriers in bulk semiconductors.[14–16,24] Under illumination with a pump laser, electrons are excited from the valence to the conduction band and consequently act as a free-carrier plasma interacting strongly with THz radiation. Optical tuning by this method has been demonstrated in silicon[14–16] and GaAs[16] where the resultant amplitude tuning is a broad band effect which decays on the order of the charge recombination time of the semiconductor material (τ_{Si} ∼100 ns, τ_{GaAs} ∼1 ns). The effect has also been employed in combination with structured illumination for wavefront shaping[24] and tunable plasmonic gratings.[25] Semiconductors have been combined with 2D materials to enhance the photo-absorption effects, where photoexcited carriers within the semiconductor diffuse into the 2D material where they experience a significantly higher mobility and therefore interact more strongly to absorb the THz radiation.[26,27] To implement further functionality into tuning devices it can be desirable to incorporate metamaterials as they have been demonstrated to allow for strong absorption with highly frequency selective spectra.[28–32] Metamaterials fabricated on semi-insulating GaAs,[33,34] silicon,[35–39] and ErAs/GaAs,[40] have been demonstrated where tuning of the substrate dielectric properties affects the plasmonic resonance of the metamaterial array.

Further, the combination of 2D materials with metamaterials and semiconductors allows to tune metamaterial resonance through optical doping of the 2D material by the semiconductor substrate.[41,42] Such mechanisms based on photo-excited charge carriers are volatile so do not persist once the illumination source is removed, it is therefore advantageous to look towards optically actuated mechanisms which are non-volatile. Phase change materials have been demonstrated as a platform for tunable non-volatile plasmonic devices, where the crystalline to amorphous transition results in substantial refractive index changes. However, optical control of phase change media requires typically complex configurations based on pulsed, high intensity laser systems.[43–47] The crystalline to amorphous transition of a phase change material results in a substantial refractive index change which can tune a resonant structure by controlling its electromagnetic environment. This mechanism does not electrically dope and therefore cannot control in a direct manner the properties of a 2D material, and furthermore phase change materials are notoriously difficult to combine with metals as they suffer from inter-diffusion which can destroy plasmonic resonant systems.[48] The mechanism proposed here can allow a platform for non-volatile control of other semiconducting 2D materials beyond graphene to enable devices with tunable frequency and strength of emission.

Here we present a non-volatile optical doping mechanism for 2D and few-atomic-layer nanomaterials based on iron doped lithium niobate (Fe:LiNbO$_3$). Fe:LiNbO$_3$ exhibits a photorefractive effect[49–51] where Fe impurities act as photoexcited donor/acceptor sites for electrons allowing the formation of optically defined charge domains within the crystal. Upon illumination electrons are excited from Fe^{+2} donor sites to the conduction band within which they are free to migrate in the crystal lattice. Under non-uniform illumination electrons will migrate from areas of high to low illumination intensity due to diffusion, becoming trapped at Fe^{+3} acceptor sites in dark regions. Alongside diffusion there is also a drift mechanism in which the photoexcited electrons are released from the donor sites with a directional preference along the direction of +z crystal axis.[51,52] There is an interplay between the two mechanisms with the drift mechanism dominating at length scales above a few microns.[53,54] Non-uniform illumination results in an optically written spatial charge distribution of arbitrary shape that depends on the illumination pattern. The spatial charge distribution is non-volatile at room temperature for long periods of time (years);[55] however it can be reversed by either thermal annealing or uniform illumination which evenly redistributes the charges within the crystal. The photoresponsive mechanism in lithium niobate is extremely versatile to implement as it is responsive to a wide frequency range in the visible spectrum (depending on choice of dopant[56]) and can be actuated by both incoherent and coherent, pulsed or continuous wave light sources. Further the speed of the photorefractive effect scales with illumination intensity[49] and can reach sub-picosecond timescales.[57,58] The ability to create photoinduced non-volatile charge distributions has led to the use of Fe:$LiNbO_3$ for recording of holograms;[59] optoelectronic tweezers for nano-objects;[60] and optical alignment of liquid crystals.[61] Recently, we suggested that iron doped lithium niobate can be employed as an optically responsive substrate for the tuning of the electrical properties of monolayer graphene[62] and demonstrated a non-volatile and reversible 2.6 fold increase of graphene resistivity under white light illumination. Here, we use this material platform to demonstrate optical control of the properties of monolayer graphene at terahertz frequencies. The system under study consists of a hybrid graphene - metal metasurface comprising an array of split-ring resonators on Fe:$LiNbO_3$ substrate (see Figure 1a). We optically define charge distributions in the substrate to locally tune the conductivity of the graphene monolayer, which controls the damping of the resonator system and thereby tunes the metamaterial resonance strength. We observe non-volatile light-induced changes in the metasurface spectral response, which are reversed by thermal annealing of the substrate. By fitting finite element calculations to the experimental results, we estimate an optically induced change in graphene charge carrier density of the order of 8×10^{11} cm^{-2}. We propose that spatially addressed frequency dependent transmission through such a device could be an invaluable tool for reconfigurable control of THz optics in applications such as wavefront shaping of beam steering. Further, we propose that the photoconductive lithium niobate platform presented here can allow for non-volatile control of a range of low dimensional semiconducting materials such as transition metal dichalcogenides which exhibit gate dependent electrical conduction and emission.[63]

2 Results and Discussion

The hybrid graphene-metal metasurface is fabricated on z-cut iron doped lithium niobate ($Fe:LiNbO_3$) single crystal substrate and a resonator array is photolithographically defined by deposition of a 5 / 100 nm Cr / Au film and subsequent lift-off process. The resonance behaviour of the metallic structure can be described well by analogy with an inductor-capacitor electrical circuit.[64] In broad terms the capacitance is inversely proportional to the split ring gap, while the inductance is related to the square of the resonator width. The device (depicted in Figure 1a) is illuminated from the top surface using a 462 nm laser source to create a non-uniform illumination within the $Fe:LiNbO_3$ substrate, which results in optically induced space-charge distributions. THz transmittance through the device is measured by Time Domain Spectroscopy (TDS) before, during, and after illumination to investigate the optical tuning of the plasmonic resonances. Figure 1(b) shows the transmittance spectrum of the device before the transfer of graphene on top of the metasurface, measured for different polarizations of the THz wave, either parallel (y) or perpendicular (x) to the split ring gap. The transmittance values are divided by transmittance through a lithium niobate substrate without metal or graphene. In the former case, we observe a pronounced resonance dip at 0.22 THz followed by a broader dip around 0.65 THz, which correspond to the fundamental and third-order resonances, respectively, while in the case of perpendicular to the gap polarization (x), the metasurface presents a broad resonance dip centred at 0.45 THz which is the second order resonance. Experimental measurements are in good agreement with finite element simulations for both polarizations (see dashed lines in Figure. 1b). Overlaid to the plot are dashed lines showing simulated transmittance spectra corresponding to a similar metamaterial unit cell on lithium niobate substrate. There is a deviation between the simulated and measured transmittance at higher frequencies, which is attributed to fabrication imperfections. Figures 1(c & e) show simulated electric field maps (without graphene) at a plane 5 μm above the metamaterial surface for the parallel to the gap polarization (y) at 0.22 and 0.65 THz, indicating magnetic dipole and electric quadrupole field configuration, with the electric field presented as a percentage of the absolute electric field propagating through air (in the absence of substrate and metal). Figure 1(d) presents similar data for 0.45 THz for the perpendicular to the gap polarization (x), where the system supports an electric dipole resonance.

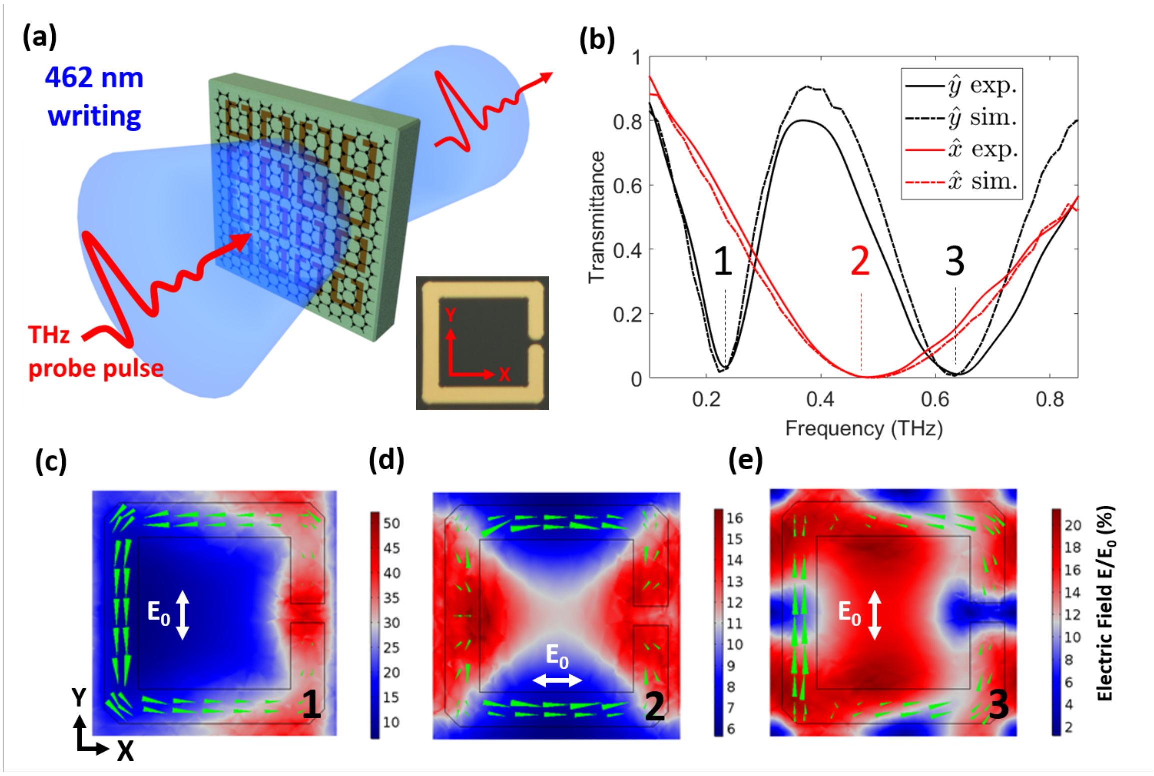

Figure 1: **(a)** Schematic showing Fe:LiNbO$_3$ substrate patterned with gold resonator array and covered in graphene. Upon illumination, electrons within the substrate are excited into the conduction band, which are then free to migrate in the crystal thus creating non-uniform charge distributions. In response to the electrostatic field created in the substrate the graphene becomes electrostatically doped, altering the Ohmic losses in the metamaterial system, altering the resonance spectra. **(b)** Experimental and simulated transmittance spectra of metallic resonators at two orientations without graphene. **(c, d & e)** Simulated electric field maps at 0.22, and 0.65 THz for the y orientation, and at 0.45 THz for the x orientation. The electric field is normalized to the amplitude of the incident field. Green arrows represent the current density in the metallic split-rings.

Figure 2 shows experimental and simulated spectra revealing photoinduced changes in the response of the hybrid graphene-metal metasurface measured with polarized THz along the y-axis (y) radiation. Figure 2(a) plots the transmittance before and after illumination. The resonant transmittance dips at 0.22 and 0.65 THz show significant damping as compared to the spectra in absence of the graphene layer (shown in Figure 1b). The resonance dips are fitted with Lorentzian functions to extract the corresponding linewidth, resonance frequency, and Q factor. Upon illumination there is additional damping of the resonant dips where the FWHM of the fundamental resonance (at 0.22 THz) is increased from 228 to 253 GHz. To assess the shape of a resonance feature the Q factor is commonly quoted, which is defined by the central frequency divided by the resonance width ($Q = f_0/\Delta f$), where the FWHM of the resonance peak is used for the resonance width Δf. As the resonance width increases at the fundamental resonance the Q factor decreases from 0.85 to 0.72, while at the third order resonance the FWHM increases from 358 to 387 GHz resulting in the Q factor decreasing from 1.75 to 1.61 as the Ohmic losses are increased due to the optically induced gating effect induced by the substrate. Overlaid in Figure 2(a) are simulated transmittance spectra, where the graphene Fermi level is modified from 0.18 to 0.20 eV. There is good agreement between the experimental and simulation except at the low frequencies where transmittance measurements in the THz TDS become sensitive to phase errors and diffraction, and high frequencies which suffer from low signal to noise ratio. Figure 2(b) presents the transmittance spectra of Figure 2(a) normalized to transmittance before illumination. Two peaks can be observed which correspond to the resonant frequencies at 0.22 and 0.65 THz, where the maximum increase in normalized transmittance reaches up to 15%. Figure 2(c) plots the normalized transmittance at the third order resonance mode (0.65 THz) while the device is under illumination. The transmittance values are normalized to transmittance before illumination and the data points are fitted with an inverse exponential equation[51] of form $T = a(1 - e^{-F/F_0}) + 1$, where T is the normalized transmittance value, a is the scaling factor = 0.19, F is the energy deposited, and F_0 is the energy required to reach to 67 % percent of saturation value, which here is equal to 11.1 J/cm^2. The saturation value $s = a + 1$ which therefore reveals the saturated normalized transmittance change of 1.19. In Figure 2(d) frequency dependent normalized transmittance values are plotted in a color map as a function of time (on the y axis). All transmittance values are normalized with respect to the "dark" values. The colour map shows that in the first 20 minutes, while the laser is off, the THz transmittance through the device is stable in dark ambient conditions. However, once the 462 nm laser source is switched on, sudden changes in transmittance occur, which are localised to two distinct frequency bands at 0.22 and 0.65 THz. After the laser is switched off, the optically induced effects persist, in the absence of illumination, highlighting the non-volatile nature of the mechanism. Figures 2(e & f) present the corresponding simulated change of the electric field ($|\overrightarrow{E_{0.2eV}}|$ - $|\overrightarrow{E_{0.18eV}}|)/|\overrightarrow{E_0}|$ above the metasurface for the first (0.22 THz) and second (0.65 THz) resonance. At the fundamental resonance (0.22 THz), the main change takes place in the vicinity of the split-ring gap, where the electric field decreases by ~ 1 %. At the third-order resonance (0.65 THz), in Figure 2(f), the electric field minimum in the gap increases, while the field maxima at the two opposite corners show a decrease in electric field, this shows a reduced contrast in electric field values. The field maps presented in Figures 2e-f can be understood in the following manner: as the Fermi level of the graphene is increased, the graphene conductivity also increases which leads to a decrease in confinement, and increase in Ohmic loss. Electric fields in regions which were previously high will be decreased, while fields in regions which were low will be increased as the plasmonic mode loses confinement. Therefore, Figures 2e-f show almost the inverse color profile to Figures 1(c) and 1(e) (which display the electric field maps without graphene).

Figure 3 presents the spectral response of the hybrid graphene metasurface measured with polarized THz along the x-axis (x). Here, the resonance centred at 0.45 THz is damped after illumination of the device, which leads to an increase of the FWHM (obtained by Lorentzian fitting) from 590 to 630 GHz and results in a Q factor decrease from 0.78 to 0.73. The corresponding normalized transmittance change (see Figure 3b) presents a resonance peak around 0.45 THz, where the optical doping effect results in an increase of 35 %. Simulated data are fitted to the transmittance spectra where a graphene Fermi level change from 0.17 to 0.20 eV provides a good agreement with experimental data. The simulated spectra show a similar shape to the experimentally measured transmittance. However, the central

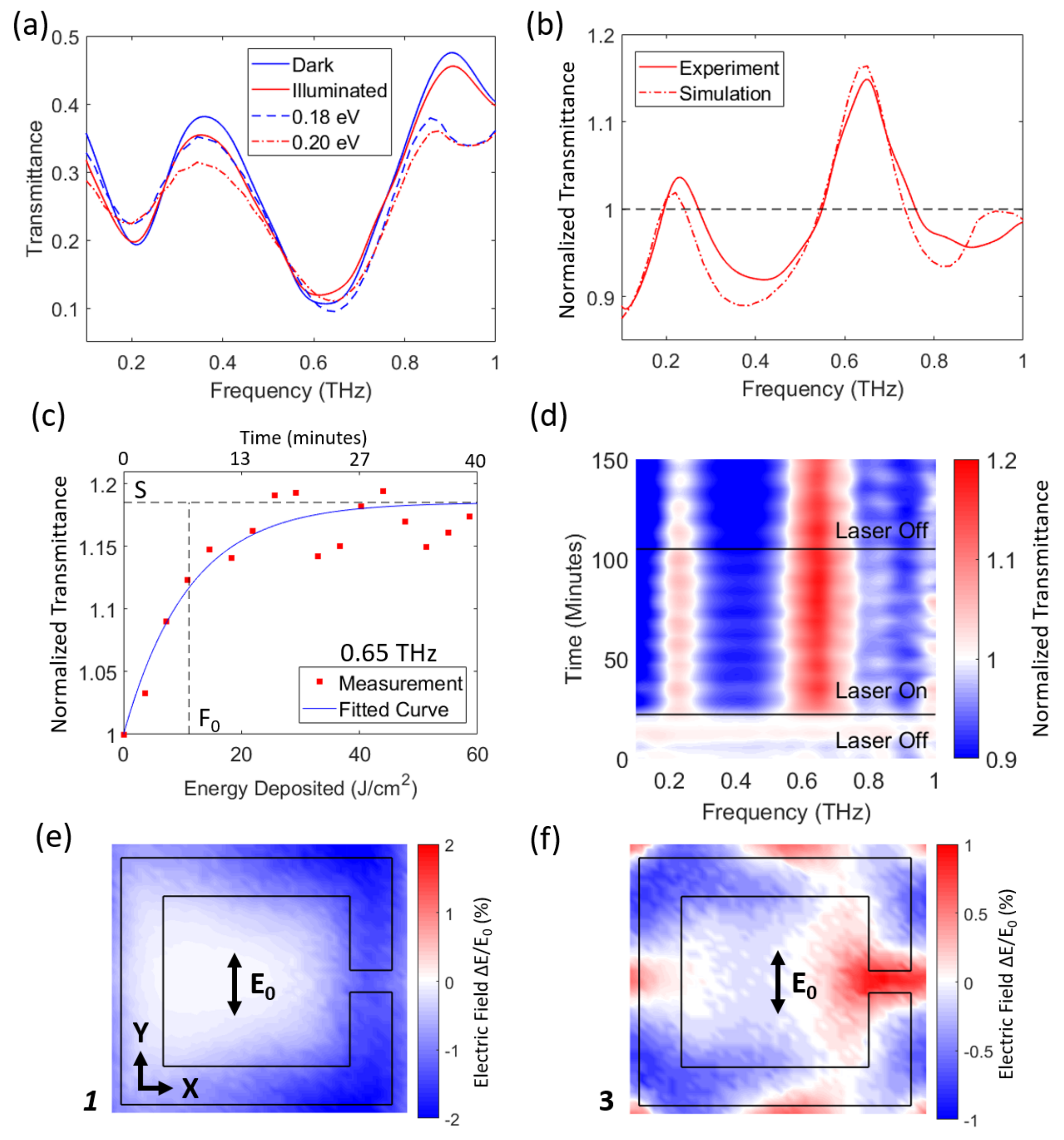

Figure 2: **(a)** Transmittance for THz radiation polarized in the y-axis (y) before (blue) and after (red) illumination (solid lines) overlayed with simulated results (dashed lines) for graphene Fermi levels of 0.18 eV (blue) and 0.20 eV (red). The experimental spectra are averaged over the "Laser On" and "Laser Off" periods. **(b)** Experimental (solid) and simulated (dashed) transmittance normalized to the transmittance before illumination. **(c)** Normalized transmittance measured at 3rd resonance mode (0.65 THz) during illumination, fitted with inverse exponential equation. **(d)** Normalized transmittance as a function of frequency and time. The transmittance is constant before illumination, however once illuminated there is a rapid change in transmittance spectra which persists once the illumination source is removed. **(e & f)** Simulated change in electric field $|\overrightarrow{E}|$ after illumination due to photoinduced change of graphene Fermi level at 0.22 (d) and 0.65 THz (e).

frequency of the resonance peak is offset by $\sim$ 45 GHz, which may be attributed to differences between the modelled resonator and the actual fabricated geometry and differences in the refractive index of the deposited gold layer. The color map in Figure 3(c) indicates that the normalized transmittance change is localised around 0.45 THz and once the illumination is removed the effect persists, while the device is held in the dark. The simulated electric field change $(|\overrightarrow{E_{0.2eV}}|$ - $|\overrightarrow{E_{0.17eV}}|)/|\overrightarrow{E_0}|$ in Figure 3(d) indicates that as the graphene Fermi level is increased, the electric field magnitude decreases at each end of the resonator as would be expected from the direction of the electric dipole.

The results presented in Figures 2(b) and 3(b) show that when measured with x and y polarized THz (corresponding to electric dipole and magnetic dipole configurations) the illumination creates distinct peaks of increased transmittance, which correspond to the resonant reflectance peaks of the metasurface. Therefore it can be understood that upon illumination the reflection resonance becomes weaker which relates to an increase in transmittance. The normalized transmittance change is highest for THz polarization in the x-axis (x), which is perhaps unexpected as it could be presumed that small changes in the graphene conductivity would result in large changes to the capacitance of the resonator gap therefore altering the y polarization by a greater degree. Our simulations indicate that the change in doping is significantly larger for the former case, which can be attributed to adsorption of atmospheric particles and moisture that can screen the electrostatic field of the substrate and dope the graphene. The measurements at different orientation are separated by several days and several thermal annealing cycles, which are likely to induce changes to the graphene layer which is responsible for the different initial Fermi levels between the two polarization's measured here. When repeat cycles of illumination followed by thermal annealing are investigated (Supplementary Figure S1) we find the normalized transmittance changes decrease with repeat cycles. Since we know $LiNbO_3$ can be re-used without degradation,[60,61] this behaviour suggests a possible degradation of the graphene layer, where changes to the electrical properties of graphene devices on ferroelectric substrates have previously been reported due to

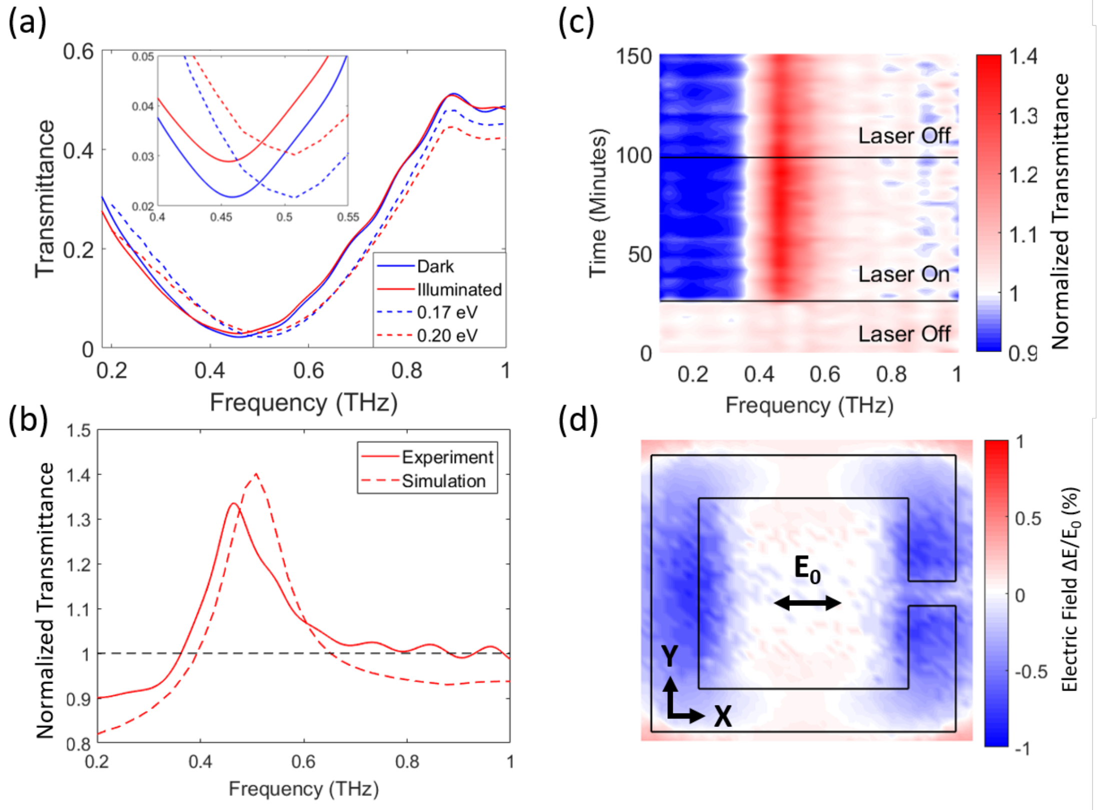

Figure 3: **(a)** Transmittance measured with THz radiation polarized in the x-axis (x) before and after laser illumination (solid lines) overlayed with simulated results (dashed lines) where graphene Fermi level is modified from 0.17 to 0.20 eV. **(b)** Experimental and simulated transmittance normalized to the spectra before illumination. **(c)** Normalized transmittance versus time color map. **(d)** Simulated change in electric field after illumination due to photoinduced change of graphene Fermi level. The electric field map is obtained by simulating the resonator covered with graphene at 0.20 eV and 0.17 eV, calculating the absolute value of the electric field $|\overrightarrow{E}|$, subtracting the electric field before the change (0.17 eV) from the electric fields after the change (0.20 eV), and then normalising all values with respect to the incident electric field.

adsorption of charged atmospheric particles.[65] To overcome this issue, future experiments will involve encapsulating the graphene with a protective layer such as hexagonal boron nitride (hBN) which could increase the long-term stability of the device. Graphene covered with hBN has been demonstrated to allow for high values of charge carrier mobility[66] and provide isolation from atmospheric chemical doping.[67] Furthermore in recent years hBN monolayers of several square centimetres have become commercially available on sacrificial polymer substrates for routine transfer processes, which indeed makes hBN encapsulation compatible with the device we present here.

Our experimental measurements (see Figs. 2c & 3c) indicate that the change in resonance spectra occurs within the first few minutes of illumination. In fact, the speed of the photorefractive effect in Fe:LiNbO$_3$ is directly proportional to the intensity of the illumination source[49] and can reach sub-picosecond timescales.[57,58] However, the limiting factor for the speed of the process here is associated with the THz data collection system, which takes some minutes to collect accurate data, and as such the device is illuminated at low intensity. Moreover, once the illumination source is removed the spectral response does not revert back to pre-illumination conditions highlighting the non-volatility of the effect. Small variations in the resonance spectra in absence of illumination can be attributed to the adsorption of atmospheric particles that compensate the electric field of the lithium niobate substrate. In Supplementary Figure S4 we plot normalized transmittance during the illumination period and for a subsequent period of 3 hours in the dark which demonstrates the non-volatility of the mechanism. There are visible fluctuations in transmittance, however when a moving average is overlaid (blue line) to the figure we see that the moving average in the post-illumination period for the two frequencies follows largely the same behaviour, suggesting this effect is due to the spectrometer.

A control experiment is performed in which a device consisting of Fe:LiNbO$_3$ with metallic metasurface array without graphene is illuminated while the THz transmittance properties are measured. The results of this control experiment (provided in Supplementary Figure

S2) reveal that in the absence of graphene there are no optically induced transmittance changes. Further, the standard deviation of the control experiment normalized transmittance is ±0.023, which demonstrates the spectrometer fluctuations are lower than the measured normalized transmittance changes in the graphene-metal metasurface devices. Finally, our results indicate that there is a significant contribution to the observed photo-induced effects from the drift mechanism in the substrate.[51,52] This is illustrated in Supplementary Figure S3, where we show reversal of the effects in metasurfaces on oppositely charged ±z Fe:$LiNbO_3$ faces. The magnitude of the transmittance changes presented here are currently limited by the design of the metallic resonator structure (which could be optimised to produce a higher Q factor resonance) and the quality of the graphene. Further, by use of an independent electrical top-gate we propose that the graphene could be brought towards the Dirac point where the graphene electrical resistivity is most sensitive to changes in charge carrier numbers. To investigate the potential for device optimisation we perform finite element simulations in which the split ring gap is reduced to 0.5 μm, and the initial Fermi level is reduced to 0.03 eV. By injection of $8{\times}10^{11}/cm^2$ charge carriers into the graphene it is shown in Supplementary Figure S5 the optically induced normalized transmittance changes reach ∼ 90% for the $\hat{y}$ polarization, and up to 80% for the $\hat{x}$ polarization. We see that in the optimised device the largest transmittance changes which can be achieved for the y orientation are at 0.3 THz where the transmittance decreases from 0.26 in dark conditions to 0.16 when illuminated.

3 Conclusion

We have demonstrated non-volatile optical tuning of a plasmonic resonator array sandwiched between monolayer graphene and a photoresponsive Fe:$LiNbO_3$ substrate. The effect is capable of producing normalized transmittance changes up to ∼35% in the device at the plasmonic resonance peak in a non-volatile manner and reversible under thermal annealing.

Finite element method simulations determine the photorefractive effect results in a charge carrier injection of 8×10^{11} cm^{-2} into the graphene. In subsequent work optical erasure methods will be investigated to remove the reliance on thermal annealing. To improve the switching capabilities of this device we propose future optimisation of the resonator geometry, and the fabrication of an electrical top-gate to bring the graphene near to the Dirac point where it is most sensitive to electrostatic gating. The ability to locally control the electrical loss in a plasmonic resonator array *via* optical illumination can allow for reconfigurable sensing and tuning applications in graphene. Further, we propose the ability to locally tune the graphene Fermi level will allow for non-volatile, yet reversible, optically defined plasmonic resonators of a graphene / Fe:LiNbO$_3$ device by optically patterning regions of high and low conductivity graphene, removing the need for permanent lithographic patterning of metallic structures. Finally we propose that the Fe:LiNbO$_3$ substrate is not limited to use only with graphene but will be applicable to tuning of a wide range of 2D or low dimensional nanomaterials such as transition metal dichalcogenides which exhibit electronic bandgaps to allow for high on-off ratio tuning of electronic conductivities.

4 Methods

Fabrication: Devices are fabricated on iron doped lithium niobate (Fe:LiNbO$_3$) crystals substrates. An array of metallic SRRs is defined by photolithography of S1813 photoresist followed by electron beam evaporation deposition of a Cr/Au stack (5/100 nm). Excess material is removed in a lift-off process in acetone to remove any metal deposited on top of the photoresist. Commercially supplied CVD graphene (grown on copper foil) is transferred *via* sacrificial polymer substrate and layered on top of the SRRs in a wet-transfer process. After transfer of the graphene the device is held under vacuum (10^{-3} mBar) for 24 hours to remove moisture under the graphene layer and promote adhesion before the removal of the protective PMMA layer *via* washing in acetone followed by isopropyl alcohol. Due to the photo-responsive nature of the substrate, the devices are thermally annealed in a convection oven at 100°C for 24 hours prior to any measurements in order to thermally redistribute any non-uniform charge distributions within the substrate.

THz Time Domain Spectroscopy: THz TDS is used to characterise the transmittance spectrum of the devices in the frequency range 0.1 to 1 THz. THz pulses are created by the optical excitation of a voltage biased photo-conductive antenna (PCA) *via* a pulsed femtosecond laser at 800 nm. The devices are measured before, during, and after illumination, then the frequency domain spectra is divided by a reference spectrum that was obtained before illumination. The division removes the effects of frequency dependant emission, propagation in air, propagation in lithium niobate, and Fresnel reflections from the air/Fe:LiNbO$_3$ interface.

Illumination: The devices are illuminated from the top surface, which is covered with the resonator array and graphene by a 462 nm fibre coupled diode laser at 25 mW cm^{-2}, collimated at the fibre output by an aspheric lens resulting in a 10 mm beam diameter as shown in Figure 1(a). The laser is aligned on the device to ensure the beam completely covers the region of the focused THz pulse; this is achieved by using a metallic aperture of diameter 3 mm at the rear surface of the device which is placed at the THz focus and visually overlapping the laser beam with the aperture. For the duration of all experiments the emitter, detector, and SRR device are held in a light-proof box to avoid ambient illumination of the device. Before illumination THz scans are taken over a 20 minute period to gauge the drift in the THz system. The device is then illuminated continuously for a 70 minute period while measuring the THz transmittance. The illumination source is then switched off and the scans continue in the dark to observe whether any optically induced transmittance change is non-volatile. As the optical beam is larger than the device we assume the illumination intensity is uniform of the area of the device, therefore the photorefractive effect will be driven by drift (along the z axis) and diffusion (to dark areas under the metallic resonators).

Charge Carrier Calculations: Charge carrier numbers can be extracted from the Fermi level values,[68] where the frequency dependent conductivity is calculated from Fermi level and the DC conductivity is obtained by multiplying by (1 - $i\omega\tau$). The carrier number n is then simply given by dividing the DC conductivity by electron charge and mobility. From this calculation we find that for a Fermi level change from 0.17 to 0.20 eV there is a carrier injection of 8×10^{11} cm^{-2} in response to the optical gating effect of the substrate under illumination.

Finite Element Analysis: A finite element analysis method is performed to show the effect of varying graphene Fermi level on the transmittance spectrum of the resonator structures. The model consists of a unit cell 50 x 50 μm in the x-y direction; linearly polarised electromagnetic radiation is excited from a port on the upper plane of the unit cell propagating downwards through 300 μm of air then into a 1 mm deep slab of lithium niobate. Experimental values of the frequency dependent complex refractive index of the $LiNbO_3$ substrate are measured in our THz TDS. A gold resonator structure is created on the air/lithium niobate interface and modelled to the 2 dimensional geometry of the photolithography mask. The permittivity values of the gold are taken from a Drude model.[69] Graphene is modelled as 3D sheet covering the entire unit cell on top of the gold resonator, which is identical to the fabricated structure. Graphene permittivity and conductivity are dependent on Fermi level and frequency, and mobility is taken as 3760 cm^{2}V^{-1}s^{-1} as quoted by the graphene manufacturer. Transmitted power is normalized against a simulation in the absence of graphene and gold through a LiNbO$_3$ slab. The simulation is first performed in the absence of the graphene layer to compare to experimental spectra before graphene transfer. The graphene layer is then added to the simulated model and the Fermi level of the graphene is modified in a parametric sweep to find convergence with experimental results.

5 Acknowledgement

We acknowledge financial support from the UK's Engineering and Physical Sciences Council through the Teranet network (grant EP/M00306X/q), and from the Quantum Hub of Sensing and Timing (EP/T001046/1). All data supporting this study are openly available from the University of Southampton repository.

6 Supporting Information Available

Repeatability investigation; multiple cycles of write, read, and erasure. Control experiment with metallic meatsurface on lithium niobate substrate without graphene. Metasurfaces fabricated on plus and minus z faces on lithium niobate to investigate effects of ferroelectric axis. This material is available free of charge *via* the Internet at http://pubs.acs.org.

References

(1) Markelz, A.; Roitberg, A.; Heilweil, E. Pulsed Terahertz Spectroscopy of DNA, Bovine Serum Albumin and Collagen between 0.1 and 2.0 THz. *Chem. Phys. Lett.* **2000**, *320*, 42 – 48.

(2) Ebbinghaus, S.; Kim, S. J.; Heyden, M.; Yu, X.; Heugen, U.; Gruebele, M.; Leit-

ner, D. M.; Havenith, M. An Extended Dynamical Hydration Shell around Proteins. *Proc. Natl. Acad. Sci. U.S.A* **2007**, *104*, 20749–20752.

(3) Walther, M.; Fischer, B.; Schall, M.; Helm, H.; Jepsen, P. Far-Infrared Vibrational Spectra of all-Trans, 9-cis and 13-cis Retinal Measured by THz Time-Domain Spectroscopy. *Chem. Phys. Lett.* **2000**, *332*, 389–395.

(4) Woodward, R. M.; Wallace, V. P.; Pye, R. J.; Cole, B. E.; Arnone, D. D.; Linfield, E. H.; Pepper, M. Terahertz Pulse Imaging of *ex vivo* Basal Cell Carcinoma. *J. Investig. Dermatol* **2003**, *120*, 72–78.

(5) Federici, J. F.; Schulkin, B.; Huang, F.; Gary, D.; Barat, R.; Oliveira, F.; Zimdars, D. THz Imaging and Sensing for Security Applications - Explosives, Weapons and Drugs. *Semicond. Sci. Technol* **2005**, *20*, S266–S280.

(6) Appleby, R.; Wallace, H. B. Standoff Detection of Weapons and Contraband in the 100 GHz to 1 THz Region. *IEEE Trans. Antennas Propag.* **2007**, *55*, 2944–2956.

(7) Chen, J.; Chen, Y.; Zhao, H.; Bastiaans, G. J.; Zhang, X.-C. Absorption Coefficients of Selected Explosives and Related Compounds in the Range of 0.1-2.8 THz. *Opt. Express* **2007**, *15*, 12060 – 12067.

(8) Wei, J.; Olaya, D.; Karasik, B. S.; Pereverzev, S. V.; Sergeev, A. V.; Gershenson, M. E. Ultrasensitive Hot-Electron Nanobolometers for Terahertz Astrophysics. *Nat. Nanotechnol* **2008**, *3*, 496–500.

(9) Negrello, M.; Hopwood, R.; Zotti, G. D.; Cooray, A.; Verma, A.; Bock, J.; Frayer, D. T.; Gurwell, M. A.; Omont, A.; Neri, R.; Dannerbauer, H.; Leeuw, L. L.; Barton, E.; Cooke, J.; Kim, S.; da Cunha, E.; Rodighiero, G.; Cox, P.; Bonfield, D. G.; Jarvis, M. J.; Serjeant, S.; Ivison, R. J.; Dye, S.; Aretxaga, I.; Hughes, D. H.; Ibar, E.; Bertoldi, F.; Valtchanov, I.; Eales, S.; Dunne, L.; Driver, S. P.; Auld, R.; Buttiglione, S.; Cava, A.;

Grady, C. A.; Clements, D. L.; Dariush, A.; Fritz, J.; Hill, D.; Hornbeck, J. B.; Kelvin, L.; Lagache, G.; Lopez-Caniego, M.; Gonzalez-Nuevo, J.; Maddox, S.; Pascale, E.; Pohlen, M.; Rigby, E. E.; Robotham, A.; Simpson, C.; Smith, D. J. B.; Temi, P.; Thompson, M. A.; Woodgate, B. E.; York, D. G.; Aguirre, J. E.; Beelen, A.; Blain, A.; Baker, A. J.; Birkinshaw, M.; Blundell, R.; Bradford, C. M.; Burgarella, D.; Danese, L.; Dunlop, J. S.; Fleuren, S.; Glenn, J.; Harris, A. I.; Kamenetzky, J.; Lupu, R. E.; Maddalena, R. J.; Madore, B. F.; Maloney, P. R.; Matsuhara, H.; Michaowski, M. J.; Murphy, E. J.; Naylor, B. J.; Nguyen, H.; Popescu, C.; Rawlings, S.; Rigopoulou, D.; Scott, D.; Scott, K. S.; Seibert, M.; Smail, I.; Tuffs, R. J.; Vieira, J. D.; van der Werf, P. P.; Zmuidzinas, J. The Detection of a Population of Submillimeter-Bright, Strongly Lensed Galaxies. *Science* **2010**, *330*, 800–804.

(10) Nagai, N.; Sumitomo, M.; Imaizumi, M.; Fukasawa, R. Characterization of Electron- or Proton-Irradiated Si Space Solar Cells by THz spectroscopy. *Semicond. Sci. Technol* **2006**, *21*, 201–209.

(11) Ahi, K.; Shahbazmohamadi, S.; Asadizanjani, N. Quality Control and Authentication of Packaged Integrated Circuits using Enhanced-Spatial-Resolution Terahertz Time-Domain Spectroscopy and Imaging. *Opt. Laser Eng.* **2018**, *104*, 274–284.

(12) Jornet, J. M.; Akyildiz, I. F. Graphene-based Plasmonic Nano-Antenna for Terahertz Band Communication in Nanonetworks. *IEEE J. Sel. Areas Commun.* **2013**, *31*, 685–694.

(13) Seeds, A. J.; Shams, H.; Fice, M. J.; Renaud, C. C. TeraHertz Photonics for Wireless Communications. *J. Light. Technol.* **2015**, *33*, 579–587.

(14) Alius, H.; Dodel, G. Amplitude-, Phase-, and Frequency Modulation of Far-Infrared Radiation by Optical Excitation of Silicon. *Infrared Phys. Technol.* **1991**, *32*, 1–11.

(15) Vogel, T.; Dodel, G.; Holzhauer, E.; Salzmann, H.; Theurer, A. High-Speed Switching

of Far-Infrared Radiation by Photoionization in a Semiconductor. *Appl. Opt.* **1992**, *31*, 329–337.

(16) Nozokido, T.; Minamide, H.; Mizuno, K. Modulation of Submillimeter Wave Radiation by Laser-Produced Free Carriers in Semiconductors. *Electr. Commun. JPN* **1997**, *80*, 1–9.

(17) Rivas, J. G.; Kuttge, M.; Kurz, H.; Bolivar, P. H.; Sánchez-Gil, J. A. Low-Frequency Active Surface Plasmon Optics on Semiconductors. *Appl. Phys. Lett.* **2006**, *88*, 082106.

(18) Han, J.; Lakhtakia, A. Semiconductor Split-Ring Resonators for Thermally Tunable Terahertz Metamaterials. *J. Mod. Opt* **2009**, *56*, 554–557.

(19) Chen, H.-T.; Padilla, W. J.; Cich, M. J.; Azad, A. K.; Averitt, R. D.; Taylor, A. J. A Metamaterial Solid-State Terahertz Phase Modulator. *Nat. Photonics* **2009**, *3*, 148–151.

(20) Kleine-Ostmann, T.; Dawson, P.; Pierz, K.; Hein, G.; Koch, M. Room-Temperature Operation of an Electrically Driven Terahertz Modulator. *Appl. Phys. Lett.* **2004**, *84*, 3555–3557.

(21) Chen, H.-T.; Padilla, W. J.; Zide, J. M. O.; Gossard, A. C.; Taylor, A. J.; Averitt, R. D. Active Terahertz Metamaterial Devices. *Nature* **2006**, *444*, 597–600.

(22) Han, Z.; Kohno, K.; Fujita, H.; Hirakawa, K.; Toshiyoshi, H. MEMS Reconfigurable Metamaterial for Terahertz Switchable Filter and Modulator. *Opt. Express* **2014**, *22*, 21326 – 21339.

(23) Tao, H.; Strikwerda, A. C.; Fan, K.; Padilla, W. J.; Zhang, X.; Averitt, R. D. Reconfigurable Terahertz Metamaterials. *Phys. Rev. Lett.* **2009**, *103*, 147401.

(24) Busch, S.; Scherger, B.; Scheller, M.; Koch, M. Optically Controlled Terahertz Beam Steering and Imaging. *Opt. Lett.* **2012**, *37*, 1391–1393.

(25) Okada, T.; Tanaka, K. Photo-Designed Terahertz Devices. *Sci. Rep.* **2011**, *1*, 121.

(26) Weis, P.; Garcia-Pomar, J. L.; Höh, M.; Reinhard, B.; Brodyanski, A.; Rahm, M. Spectrally Wide-Band Terahertz Wave Modulator Based on Optically Tuned Graphene. *ACS Nano* **2012**, *6*, 9118–9124.

(27) Chen, S.; Fan, F.; Miao, Y.; He, X.; Zhang, K.; Chang, S. Ultrasensitive Terahertz Modulation by Silicon-Grown $\mathrm{MoS_2}$ Nanosheets. *Nanoscale* **2016**, *8*, 4713–4719.

(28) Wu, P.; Zhang, C.; Tang, Y.; Liu, B.; Lv, L. A Perfect Absorber Based on Similar Fabry-Perot Four-Band in the Visible Range. *Nanomaterials* **2020**, *10*, 488.

(29) Wu, P.; Chen, Z.; Jile, H.; Zhang, C.; Xu, D.; Lv, L. An infrared perfect absorber based on metal-dielectric-metal multi-layer films with nanocircle holes arrays. *Results Phys.* **2020**, *16*, 102952.

(30) Li, J.; Chen, X.; Yi, Z.; Yang, H.; Tang, Y.; Yi, Y.; Yao, W.; Wang, J.; Yi, Y. Broadband solar energy absorber based on monolayer molybdenum disulfide using tungsten elliptical arrays. *Mater. Today* **2020**, *16*, 100390.

(31) Li, J.; Chen, Z.; Yang, H.; Yi, Z.; Chen, X.; Yao, W.; Duan, T.; Wu, P.; Li, G.; Yi, Y. Tunable Broadband Solar Energy Absorber Based on Monolayer Transition Metal Dichalcogenides Materials Using Au Nanocubes. *Nanomaterials* **2020**, *10*, 257.

(32) Qi, Y.; Zhang, Y.; Liu, C.; Zhang, T.; Zhang, B.; Wang, L.; Deng, X.; Wang, X.; Yu, Y. A Tunable Terahertz Metamaterial Absorber Composed of Hourglass-Shaped Graphene Arrays. *Nanomaterials* **2020**, *10*, 533.

(33) Padilla, W. J.; Taylor, A. J.; Highstrete, C.; Lee, M.; Averitt, R. D. Dynamical Electric and Magnetic Metamaterial Response at Terahertz Frequencies. *Phys. Rev. Lett.* **2006**, *96*, 107401.

(34) Manceau, J. M.; Shen, N. H.; Kafesaki, M.; Soukoulis, C. M.; Tzortzakis, S. Dynamic Response of Metamaterials in the Terahertz Regime: Blueshift Tunability and Broadband Phase Modulation. *Appl. Phys. Lett.* **2010**, *96*, 021111.

(35) Chowdhury, D. R.; Singh, R.; O'Hara, J. F.; Chen, H. T.; Taylor, A. J.; Azad, A. K. Dynamically Reconfigurable Terahertz Metamaterial through Photo-Doped Semiconductor. *Appl. Phys. Lett.* **2011**, *99*, 231101.

(36) Chen, H. T.; O'Hara, J. F.; Azad, A. K.; Taylor, A. J.; Averitt, R. D.; Shrekenhamer, D. B.; Padilla, W. J. Experimental Demonstration of Frequency-Agile Terahertz Metamaterials. *Nat. Photonics* **2008**, *2*, 295–298.

(37) Gu, J. Q.; Singh, R.; Liu, X. J.; Zhang, X. Q.; Ma, Y. F.; Zhang, S.; Maier, S. A.; Tian, Z.; Azad, A. K.; Chen, H. T.; Taylor, A. J.; Han, J. G.; Zhang, W. L. Active Control of Electromagnetically Induced Transparency Analogue in Terahertz Metamaterials. *Nat. Commun.* **2012**, *3*, 1151.

(38) Hendry, E.; Lockyear, M. J.; Rivas, J. G.; Kuipers, L.; Bonn, M. Ultrafast Optical Switching of the THz Transmission through Metallic Subwavelength Hole Arrays. *Phys. Rev. B* **2007**, *75*, 235305.

(39) Janke, C.; Rivas, J. G.; Bolivar, P. H.; Kurz, H. All-Optical Switching of the Transmission of Electromagnetic Radiation through Subwavelength Apertures. *Opt. Lett.* **2005**, *30*, 2357–2359.

(40) Chen, H. T.; Padilla, W. J.; Zide, J. M. O.; Bank, S. R.; Gossard, A. C.; Taylor, A. J.; Averitt, R. D. Ultrafast Optical Switching of Terahertz Metamaterials Fabricated on ErAs/GaAs Nanoisland Superlattices. *Opt. Lett.* **2007**, *32*, 1620–1622.

(41) Zheng, W.; Fan, F.; Chen, M.; Chen, S.; Chang, S. J. Optically Pumped Terahertz Wave Modulation in MoS_2-Si Heterostructure Metasurface. *AIP Adv.* **2016**, *6*, 075105.

(42) Arezoomandan, S.; Gopalan, P.; Tian, K.; Chanana, A.; Nahata, A.; Tiwari, A.; Sensale-Rodriguez, B. Tunable Terahertz Metamaterials Employing Layered 2-D Materials Beyond Graphene. *J. Sel. Top. Quantum Electron* **2017**, *23*, 188–194.

(43) Gholipour, B.; Zhang, J.; MacDonald, K. F.; Hewak, D. W.; Zheludev, N. I. An All-Optical, Non-volatile, Bidirectional, Phase-Change Meta-Switch. *Adv. Mater* **2013**, *25*, 3050–3054.

(44) Wang, Q.; Rogers, E. T.; Gholipour, B.; Wang, C.-M.; Yuan, G.; Teng, J.; Zheludev, N. I. Optically Reconfigurable Metasurfaces and Photonic Devices based on Phase Change Materials. *Nat. Photonics* **2016**, *10*, 60–65.

(45) Wuttig, M.; Bhaskaran, H.; Taubner, T. Phase-Change Materials for Non-Volatile Photonic Applications. *Nat. Photonics* **2017**, *11*, 465–476.

(46) Pitchappa, P.; Kumar, A.; Prakash, S.; Jani, H.; Venkatesan, T.; Singh, R. Chalcogenide Phase Change Material for Active Terahertz Photonics. *Adv. Mater* **2019**, *31*, 1808157.

(47) Jeong, Y.-G.; Bahk, Y.-M.; Kim, D.-S. Dynamic Terahertz Plasmonics Enabled by Phase-Change Materials. *Adv. Opt. Mater* **2019**, *8*, 1900548.

(48) Lu, L.; Dong, W.; Behera, J. K.; Chew, L.; Simpson, R. E. Inter-diffusion of plasmonic metals and phase change materials. *J. Mater. Sci.* **2018**, *54*, 2814–2823.

(49) Gunter, P.; Huignard, J. P. *Photorefractive Materials and Their Applications 1*; Springer, 2006.

(50) Weis, R. S.; Gaylord, T. K. Lithium Niobate - Summary of Physical Properties and Crystal Structure. *Appl. Phys. A* **1985**, *37*, 191–203.

(51) Puerto, A.; Munoz-Martin, J. F.; Mendez, A.; Arizmendi, L.; Garcia-Cabanes, A.; Agullo-Lopez, F.; Carrascosa, M. Synergy Between Pyroelectric and Photovoltaic Effects for Optoelectronic Nanoparticle Manipulation. *Opt. Express* **2019**, *27*, 804–815.

(52) Buse, K. Light-Induced Charge Transport Processes in Photorefractive Crystals I: Models and Experimental Methods. *Appl. Phys. B* **1997**, *64*, 273–291.

(53) Prokhorov, A. M.; Kuzminov, Y. S. *Physics and Chemistry of Crystalline Lithium Niobate*; IOP Publishing, 1990.

(54) Ohmori, Y.; Yasojima, Y.; Inuishi, Y. Photoconduction, Thermally Stimulated Luminescence, and Optical Damage in Single Crystal of $\mathrm{LiNbO_3}$. *Jpn. J. Appl. Phys* **1975**, *14*, 1291–1300.

(55) Arizmendi, L.; Lopez-Barbera, F. J. Lifetime of Thermally Fixed Holograms in $\mathrm{LiNbO_3}$ Crystals Doped with Mg and Fe. *Appl. Phys. B* **2007**, *86*, 105–109.

(56) Furukawa, Y.; Kitamura, K.; Ji, Y.; Montemezzani, G.; Zgonik, M.; Medrano, C.; Günter, P. Photorefractive Properties of Iron-Doped Stoichiometric Lithium Niobate. *Opt. Lett.* **1997**, *22*, 501–503.

(57) Hsieh, H.-T.; Psaltis, D.; Beyer, O.; Maxein, D.; von Korff Schmising, C.; Buse, K.; Sturman, B. Femtosecond Holography in Lithium Niobate Crystals. *Opt. Lett.* **2005**, *30*, 2233–2235.

(58) Paipulas, D. Local Photorefractive Modification in Lithium Niobate Using Ultrafast Direct Laser Write Technique. *J. Laser Micro. Nanoen.* **2016**, *11*, 246–252.

(59) Buse, K.; Adibi, A.; Psaltis, D. Non-Volatile Holographic Storage in Doubly Doped Lithium Niobate Crystals. *Nature* **1998**, *393*, 665–668.

(60) Carrascosa, M.; Garcia-Cabanes, A.; Jubera, M.; Ramiro, J. B.; Agullo-Lopez, F. $\mathrm{LiNbO_3}$: A Photovoltaic Substrate for Massive Parallel Manipulation and Patterning of Nano-Objects. *Appl. Phys. Rev* **2015**, *2*, 040605.

(61) Lucchetti, L.; Kushnir, K.; Reshetnyak, V.; Ciciulla, F.; Zaltron, A.; Sada, C.; Simoni, F. Light-Induced Electric Field Generated by Photovoltaic Substrates Investigated through Liquid Crystal Reorientation. *Opt. Mater.* **2017**, *73*, 64–69.

(62) Gorecki, J.; Apostolopoulos, V.; Ou, J. Y.; Mailis, S.; Papasimakis, N. Optical Gating of Graphene on Photoconductive Fe:LiNbO$_3$. *ACS Nano* **2018**, *12*, 5940–5945.

(63) Xiao, J.; Zhao, M.; Wang, Y.; Zhang, X. Excitons in atomically thin 2D semiconductors and their applications. *Nanophotonics* **2017**, *6*, 1309–1328.

(64) Jeppesen, C.; Mortensen, N. A.; Kristensen, A. Capacitance tuning of nanoscale split-ring resonators. *Appl. Phys. Lett.* **2009**, *95*, 193108.

(65) Rogers, S. P.; Xu, R.; Pandya, S.; Martin, L. W.; Shim, M. Slow Conductance Relaxation in Graphene–Ferroelectric Field-Effect Transistors. *J. Phys. Chem. C* **2017**, *121*, 7542–7548.

(66) Geim, A. K.; Grigorieva, I. V. Van der Waals heterostructures. *Nature* **2013**, *499*, 419–425.

(67) Mayorov, A. S.; Gorbachev, R. V.; Morozov, S. V.; Britnell, L.; Jalil, R.; Ponomarenko, L. A.; Blake, P.; Novoselov, K. S.; Watanabe, K.; Taniguchi, T.; Geim, A. K. Micrometer-Scale Ballistic Transport in Encapsulated Graphene at Room Temperature. *Nano Letters* **2011**, *11*, 2396–2399.

(68) Boggild, P.; Mackenzie, D. M. A.; Whelan, P. R.; Petersen, D. H.; Due Buron, J.; Zurutuza, A.; Gallop, J.; Hao, L.; Jepsen, P. U. Mapping the Electrical Properties of Large-Area Graphene. *2D Mater.* **2017**, *4*, 042003.

(69) Palik, E. D. *Handbook of Optical Constants of Solids*; Academic Press, 1997.

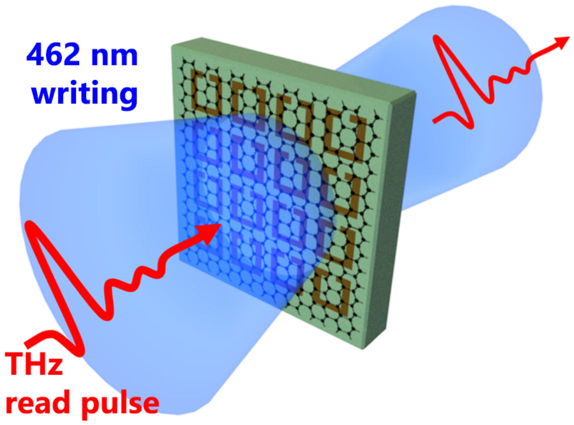
462 nm
writing
THz
read pulse

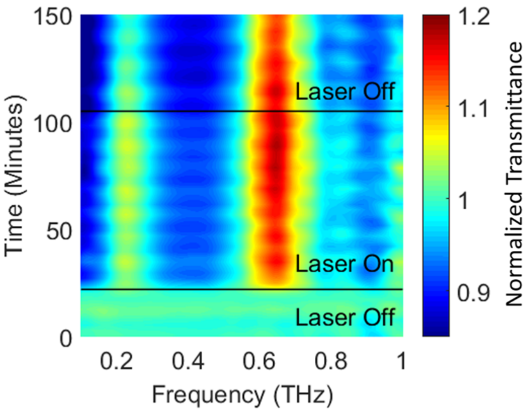
150
100
50
0
Time (Minutes)
Laser Off
Laser On
Laser Off
0.2
0.4
0.6
0.8
1
Frequency (THz)
1.2
1.1
1
0.9
Normalized Transmittance